Optical trapping with planar silicon metalenses

GEORGIY TKACHENKO[1], DAAN STELLINGA[2], ANDREI RUSKUC[2,3], MINGZHOU CHEN[1], KISHAN DHOLAKIA[1,*], AND THOMAS F. KRAUSS[2]

[1] SUPA, School of Physics and Astronomy, University of St. Andrews, KY16 9SS, UK
[2] Department of Physics, University of York, Heslington, YO10 5DD, UK
[3] California Institute of Technology, Pasadena, CA 91125, USA
[*] Corresponding author: kd1@st-andrews.ac.uk

Compiled July 31, 2018

Contactless manipulation of micron-scale objects in a microfluidic environment is a key ingredient for a range of applications in the biosciences, including sorting, guiding and analysis of cells and bacteria. Optical forces are powerful for this purpose but typically require bulky focusing elements to achieve the appropriate optical field gradients. To this end, realizing the focusing optics in a planar format would be very attractive and conducive to integration of such microscale devices either individually or as arrays. Here, we report on the first experimental demonstration of optical trapping in water using planar silicon metalenses illuminated with a collimated laser beam. The structures consist of high-contrast gratings with a locally varying period and duty-cycle. They are designed to mimic parabolic reflectors with a numerical aperture of 0.56 at a vacuum wavelength of 1064 nm. We achieve both two and three-dimensional trapping, with the latter realized by omitting the central Fresnel zones. The study highlights the versatility of such lithographically defined metastructures for exerting optical forces without the need for traditional optical elements.

OCIS codes: (140.7010) Laser trapping; (350.4855) Optical tweezers or optical manipulation; (050.1950) Diffraction gratings.

http://dx.doi.org/10.1364/ol.XX.XXXXXX

Optical trapping of micron-sized objects with a single beam in 3D requires tight focusing of light, which can be achieved by optical elements with a high numerical aperture (NA) [1]. Traditional glass lenses and microscope objectives are typically used to achieve such focusing, but they are bulky and cannot be easily integrated into lab-on-a-chip systems, which are a prime domain for optical trapping aimed at micromanipulation and analysis of cells and bacteria. An elegant solution to this problem has been the use of submillimeter-size spherical lenses [2] or reflectors [3]. These have achieved NA = 0.96 and 3D optical trapping of polystyrene beads in a microfluidic environment. However, such optical elements are typically limited to spherical shapes and thus are unable to generate anything other than

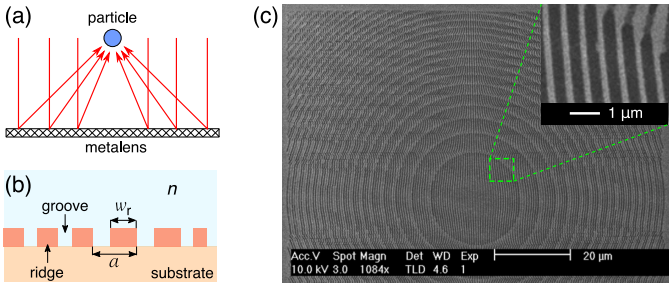

Fig. 1. (a) Principle of optical trapping with a planar metalens. (b) HCG in detail, where a is the local period, w_r – the local ridge width. (c) SEM micrograph of a fabricated metalens where light areas denote ridges, dark ones are grooves.

standard Gaussian beam traps. Moreover, they have significant relief measuring hundreds of microns, which adds up to the form factor of the end device. In this context, one would wish for an entirely planar structure capable of focusing light from a collimated incident beam into a tight spot, with the flexibility of design and the prospect of generating traps with structured beams [4]. Naturally, a homogeneous flat surface cannot create the required beam shaping, yet this task may be accomplished with metasurfaces [5–8] following the concept shown in Fig. 1(a). Realization of optical trapping with metasurface-based lenses has been challenging because (i) the requirement to operate in a fluid significantly limits the refractive index contrast and thus the focusing efficiency; (ii) even though technically, the NA may be high enough, the intensity of the high-angle beams at the periphery of the lens is usually too low. In this Letter we report on the first experimental demonstration of optical trapping with planar metalenses.

In order to avoid spherical aberrations, which are detrimental to optical trapping, particularly along the optical axis, a perfect metalens with a focal distance f should have a parabolic phase profile

$$\Phi(r) = \frac{2\pi}{\lambda}\left(\sqrt{r^2+f^2} - f\right), \quad (1)$$

where r is the distance from the center and λ is the operating wavelength. Such a lens has $\mathrm{NA}(r) = n\sin\left(\tan^{-1}(r/f)\right)$ with n being the refractive index of the medium.

Parabolic phase profiles can be created by a high-contrast grat-

ing (HCG) which is a metasurface with a subwavelength landscape of alternating ridges and grooves on a planar substrate, see Fig. 1(b),(c). The function of such a grating is determined by the interplay of guided modes with radiation modes [9]. The phase map imposed by the HCG is defined by the spatial distribution of the local period a and the duty cycle $DC = w_r/a$, where w_r is the local width of ridges. An HCG becomes a fully functional beam shaping element when it can cover the full phase range of 2π. Rigorous coupled wave analysis [10] allows us to simulate the phase and efficiency (that is transmittance or reflectance, depending on the chosen operation mode) for all possible combinations of a and DC. Subsequently, an optimum path in the (a, DC) space has to be chosen so that the 2π phase range could be covered with maximum net efficiency, see our earlier work [11] for more details.

Previously, we have demonstrated planar metalenses mimicking a parabolic reflector with NA reaching 0.93 [12]. However, optical trapping with such metalenses could not be achieved because of the low reflection efficiency in the high-order Fresnel zones, which are indispensable for the tight focusing of light. Indeed, the higher the order, the narrower the corresponding zone, as one can see in Fig. 1(c). At some point, the grating discretization becomes comparable with the Fresnel zone width, and consequently the reflection efficiency for high r/f decreases dramatically. To overcome this problem, we have now implemented a boundary condition to the design of the path in the (a, DC) space, namely that each Fresnel zone must be represented by at least three grating periods, the number of periods being defined as

$$N = \frac{1}{\bar{a}}\left(r - \sqrt{\left(r^2 + \lambda^2 - 2\lambda\sqrt{r^2+f^2}\right)}\right), \qquad (2)$$

where $\bar{a}$ is the average period for the chosen path. Eq.2 is delivered from Eq. 1 by expressing the phase change for a Fresnel zone located at the radius r as $\Phi(r) - \Phi(r - N\bar{a}) = 2\pi$. Since we expect planar metalenses to be applied for optical trapping in a microfluidic environment, we specifically designed them for operation in water ($n \approx 1.33$) at the widely used free-space wavelength $\lambda = 1064$ nm. The gratings are fabricated by direct-write electron beam lithography from a sub-micron film of crystalline silicon bonded to a glass substrate, using the same process as in [12]. For a metalens operating in reflection at normal incidence and in TM polarization (having electric field perpendicular to the grating lines), the optimum path in the (a, DC) space corresponds to $\bar{a} \approx 0.64\,\mu$m and a silicon film thickness of $0.38\,\mu$m. When the above mentioned boundary condition $N \geq 3$ is stipulated, the NA of a metalens is limited to approximately 0.6. In practice, we have chosen a lens size of $100\,\mu\text{m} \times 100\,\mu$m and a focal length of $f = 108\,\mu$m corresponding to $NA \approx 0.56$.

The focal spots created by the metalenses are characterized using an optical setup shown in Fig. 2(a). After being deflected by a shortpass dichroic mirror (DM, Thorlabs DMSP 1000R), a collimated Gaussian beam ('input beam') from a fiber laser (IPG Photonics, cw at λ =1064 nm, beam diameter 5 mm) is relayed to the sample plane in order to coaxially illuminate a single metalens at normal incidence. The relay telescope consisting of a biconvex lens (L, focal length 75 mm) and a water immersion microscope objective (MO, Nikon Fluor 60×/1.00W) reduces the beam diameter to $130\,\mu$m. The focal plane of the objective coincides with that of the metalens. The light focused by the metalens is collected and imaged by means of a camera (C, Basler pilot piA640-210gm) located at the back focal plane of lens L.

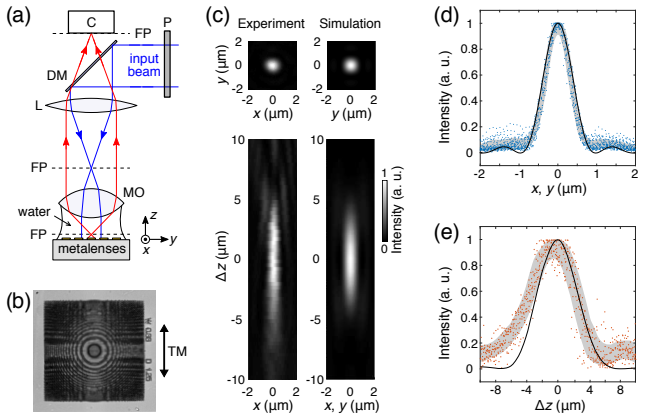

Fig. 2. Focal spot characterization. (a) Optical setup; dashed lines indicate the focal planes (FP). (b) Optical image of a metalens; the arrow shows the incident electric field orientation for TM polarization. (c) Sample transverse and axial intensity profiles of the focal spot; the color bar is common. (d),(e) Normalized intensity profiles measured (dots) and simulated (solid curve) in the transverse ((d), at $\Delta z = 0$) and axial ((e), at $x = y = 0$) cross sections of the focal spot. Grey areas denote the standard deviation ranges of the experimental data.

The linear polarizer (P) sets the input beam to either TE or TM polarization, the latter being indicated by the arrow in Fig. 2(b).

Each focal spot is considered in the Cartesian coordinate frame (x, y, z) with z indicating the propagation direction of the reflected light and the metalens located in the $z = 0$ plane. The camera is displaced along z covering the $80\,\mu$m long distance centered on $z = f$. Fig. 2(c, top left) depicts the camera image with the maximum intensity level (captured at $z \approx f$). Fig. 2(c, bottom left) is the a sample intensity map compiled from the camera images at the axial locations $\Delta z = z - f$. We simulate the electric field distribution at the focal spot by means of the Rayleigh-Sommerfeld diffraction integral with the initial phase front $\Phi(r)$ described by Eq. 1, where $r^2 = x^2 + y^2$. The simulated transverse (at $\Delta z = 0$) and axial (at $y = 0$) intensity profiles are presented in Fig. 2(c, right).

We have characterized eight different metalenses for both TE and TM polarization states. The measured transverse and axial profiles of the focal spots in each case are summarized in Figs. 2(d, e). We found that normalized intensity profiles did not depend on the polarization. We attribute the asymmetry of the measured axial profiles (Fig. 2(e)) to the spherical aberrations in the imaging system. The simulated beam waist radius (obtained by fitting to a Gaussian distribution) at $\Delta z = 0$ equals $0.67\,\mu$m, which is within the confidence range of the measured beam waist radius equal to $0.66 \pm 0.05\,\mu$m. We note that a high-NA lens is commonly characterized by the Airy disc radius (which equals 0.95 for the simulated curve in Fig. 2(d)). However, since the function of metalenses in this work is not to image but to trap particles, treating the focal spot as a Gaussian beam is more relevant for the following reasons. First, position fluctuations of a particle around an optical trap are usually 1-2 orders of magnitude smaller than fluctuations of the beam size, thus the structure of the Airy diffraction pattern beyond the full width at half-maximum is not important in the context of optical manipulation. The second reason is related to the power measurements described below.

In addition to characterising the focal spot, the camera im-

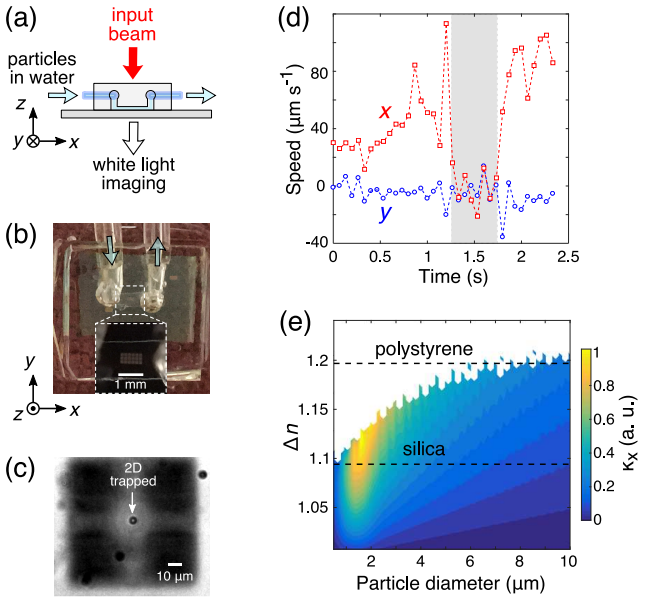

Fig. 3. 2D optical trapping. (a) Setup. (b) Microfluidic chamber with the flow directed towards $x > 0$. The expanded image shows a 3×6 array of planar metalenses visible as faint rectangles. (c) A video frame showing several polystyrene microparticles, one of which is trapped at the metalens focus (Visualization 1). (d) Typical lateral speed of a tracked microparticle passing through a metalens focus, with the gray region outlining the interval of 2D trapping. (e) Simulated lateral trap stiffness landscape whereby the white region represents the absence of axial equilibrium.

ages captured at $\Delta z = 0$ allowed us to measure the efficiency of the planar metalenses. The sum of the pixel intensity $I(x,y)$ over the image is proportional to the optical power in the image plane, as long as the beam spot fits into the screen, the exposure time is kept constant, there is no saturation, and the background is subtracted. In order to avoid a noise buildup produced by the marginal pixels of low intensity, we defined the relative power in the image plane as $P = I_0 \int_{-\infty}^{+\infty} \exp(-2(x^2+y^2)/w_0^2)\, dxdy = I_0 \pi w_0^2/2$, where I_0 and w_0 are the peak intensity and waist radius of the Gaussian beam found as the best fit to the focal spot. This optical power is referenced to the input power P_0 measured in the same fashion with the metalens being replaced by a nearly perfect broadband dielectric mirror (Thorlabs, BB1-E03). We note that P_0 has to be multiplied by $\xi = \mathrm{erf}(b/(\sqrt{2}w))^2 \approx 0.31$ in order to account for the power loss at transmission through a square aperture with a side $b = 100\,\mu$m. The metalens efficiency is estimated as $P/(\xi P_0)$ which gives $73 \pm 14\%$ for TM and $14 \pm 4\%$ for TE polarization states (six different metalenses have been tested).

The optical trapping experiments were performed in a microfluidic environment by means of the setup sketched in Fig. 3(a). The 'input beam' is the same as in the characterization setup, except for the diameter which is now reduced to 1.6 mm. Metalenses located at $z = 0$ are illuminated at normal incidence and TM polarization. The incident optical power is 1 W, which corresponds to about 10 mW across the area of a $100\,\mu\text{m} \times 100\,\mu$m metalens. The lenses are enclosed in a rectangular microchannel (1.5 mm wide and 140 μm high) molded in polydimethylsiloxane (PDMS), see Fig. 3(b). Polystyrene microparticles (diameter $5 \pm 0.3\,\mu$m) dispersed in deuterium oxide (D_2O, which is used in order to avoid the convection effects due to absorption of the laser beam) are injected into the channel by a microsyringe (Nanofil, World Precision Instruments) and move towards $x > 0$ in a quasi-laminar flow. In order to deduce trajectories and speed of the particles in the (x,y) plane, we analyzed their images (see Fig. 3(c) and Visualization 1) captured in transmission by a home-made microscope (Mitutoyo M Plan Apo $20\times/0.42$ objective, the same video camera as before, white light illumination along $z < 0$).

A particle is considered trapped when its velocity both in x and y direction oscillates around zero, see Fig. 3(d). In practice, a particle typically stays captured in the focal spot of a metalens for about 0.5 s and then resumes the motion along $x > 0$ (Visualization 1). While trapped, the particle exhibits vertical (towards $z > 0$) motion, which suggests that the optical potential provides restoring forces only in 2D. In such a potential, a particle moves under the unbalanced scattering optical force until the transverse gradient forces get too weak to compensate the flow. The latter pushes the particle off the axis of the focal spot, thus decreasing the scattering force and perhaps making the trapping state lasting slightly longer. However, understanding the exact role played by the flow would require simulations which are beyond the scope of this work.

To estimate the maximum trap efficiency, $Q^{\max}$, of the observed 2D trapping, we used the viscous drag force method: $Q^{\max} = F^{\max}\mathrm{c}/(nP) = \mathrm{c}(6\pi\eta R v_{\max})/(nP)$, where $F^{\max}$ is the maximum lateral radiation force exerted on the particle, c is the speed of light in vacuum, η is the fluid dynamic viscosity, R is the particle radius, $v_{\max}$ is the maximum flow velocity at which the particle remains trapped. We obtained $v_{\max} \approx 80\,\mu\text{m s}^{-1}$ and the corresponding efficiency $Q^{\max} \approx 0.12$, which is typical for a single-beam optical tweezer and approximately twice smaller than the values achieved with high-NA reflective spherical microlenses [3].

In fact, the absence on 3D trapping is expected given the relatively low NA of the lens and the refractive index ratio $\Delta n = n_p/n$ between the particles (n_p) and the surrounding medium (n). As follows from optical force calculations based on the generalized Lorenz-Mie theory [13], a Gaussian-like beam with $\lambda = 1064$ nm and NA $= 0.56$ can provide 3D trapping of a 5 μm uniform dielectric sphere only if the index ratio does not exceed $(\Delta n)_{\max} \approx 1.165$ (see Fig. 3(e)), whereas for polystyrene in water $(\Delta n)_{\text{poly}} \approx 1.195$. Silica particles correspond to $(\Delta n)_{\text{silica}} \approx 1.095 < (\Delta n)_{\max}$ and thus can be stably trapped at this NA. However, our attempts to achieve trapping of silica particles in a microfluidic channel were unsuccessful. The reason is their high density, which is over 2.5 times larger than that of water or polystyrene. As a result of their negative buoyancy, silica particles were either adhering to the metastructure, or flowing past the focal spots too quickly to be captured by optical forces.

As a next logical step, we have extended our study to explore 3D trapping of polystyrene particles using the planar metalenses. An obvious solution is to increase their NA. However, this would require to drop the $N \geq 3$ boundary condition for outer Fresnel zones and, therefore, would lead to the loss of accuracy in mimicking the target phase profile $\Phi(r)$. Instead, we retained the boundary condition (and the maximum NA) and omitted some of the central Fresnel zones (as shown in Fig. 4(a)) which are responsible for the major part of the axial optical force on the particle. This strategy has already proved successful for the trapping of airborne particles (that is $\Delta n \approx 1.5$) with a single laser beam shaped into a cone with maximum numerical

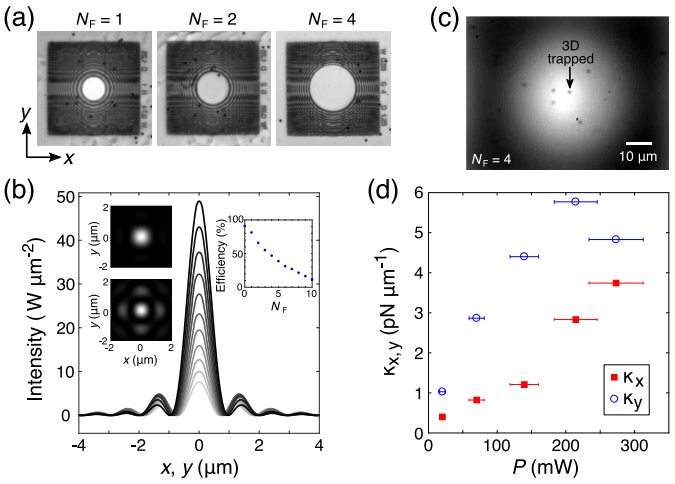

Fig. 4. 3D optical trapping. (a) Hollow planar metalenses with $N_F = 1$, 2 and 4 first Fresnel zones skipped. Dark circles are 2 μm polystyrene beads. (b) Simulated transverse intensity distribution in the focus of hollow metalenses illuminated by a collimated Gaussian beam with diameter 200 μm and power 1 W. Lighter shades of gray correspond to higher N_F values. Left insets: transverse intensity profiles for a complete metalens (top) and a hollow metalens with $N_F = 10$. Right inset: metalens efficiency versus N_F. (c) A video frame showing a polystyrene microparticle trapped in the focus of a hollow metalens ($N_F = 4$). The 3D trapping can be verified by observing surrounding particles (Visualization 2). (d) Lateral trap stiffness measured for a 2 μm polystyrene particle trapped by a hollow metalens with $N_F = 4$.

aperture of 0.6 [14]. We denote the number of skipped Fresnel zones (being counted from the center) as N_F. The total number of Fresnel zones for the 100 μm lens is $N_F^{tot} = 14$. The increase of N_F results in squeezing of the angular range for the wave vectors in the reflected field. Correspondingly, the transverse intensity profile of the focal spot resembles that of a Bessel beam where the field energy is distributed over multiple concentric rings, as shown in Fig. 4(b).

The metalens with $N_F = 4$ and polystyrene spherical microparticles of diameter 2 μm provided the best experimental results. We used an input beam of diameter 374 μm, resulting in an input power onto the metalens of the order of 100 mW. The motion of the trapped particle in the (x, y) plane was analyzed from a video recording (1500 frames captured at 33 fps). Fig. 4(c) represents a typical camera frame where a 3D trapped polystyrene microparticle appears along with the non-trapped ones with the blurred hollow metalens visible in the background. This picture is complemented by Visualization 2 where the trapped particle is exhibiting typical random motion around the optical trap center. The important evidence for 3D trapping is the motion of the non-trapped particles which may travel for significant distances along the z axis (as confirmed by the blurring of their images).

The lateral trap stiffness κ_i with $i = x, y$ is estimated by means of a standard method based on the equipartition theorem: $\kappa_i = k_B T/\sigma_i^2$, where k_B is the Boltzmann constant, T the absolute temperature in the trap (we consider $T = 294$ K for any optical power), and σ_i^2 is the variance of the particle location along i axis. Experimental results for lateral trap stiffness $\kappa_{x,y}$ vs. optical power P are shown in Fig. 4(e); the stiffness per unit power was found to be 13.54 ± 2.72 pN μm^{-1} W^{-1} and 33.70 ± 9.17 pN μm^{-1} W^{-1} for x and y directions, respectively. Such modest stiffness values are an order of magnitude smaller than those typically achieved with standard optical tweezers having high-NA objectives but may be improved in future studies with more optimal grating designs.

In summary, we have demonstrated the first use of planar metalenses to create optical traps in a microfluidic environment. By maximizing the NA and focusing efficiency and by removing the inner Fresnel zones, we were able to observe 3D trapping using this system. We believe that planar focusing metastructures may replace conventional objective lenses in lab-on-a-chip devices and other miniaturized environments where optical manipulation is desired.

Importantly, metalenses offer flexibility in the phase profile design and thus may lead far beyond simple focusing of light. To support this statement, here we have demonstrated the creation of a conical beam which enabled us to trap particles even with otherwise insufficient numerical aperture. Normally, such beam shaping would require macroscopic optical elements like ring apertures, conical lenses [14] or computer generated holograms. Besides biomedical systems, we envisage metasurface-based beam shapers to be applied for generation of complex trapping potentials for single atoms. Indeed, such microscale devices can be placed directly at the atom cloud, thus providing competition for the established macroscopic techniques [15].

We thank the UK Engineering and Physical Sciences Research Council for funding from grants EP/J01771X/1 and EP/P030017/1. We also acknowledge Blair Kirkpatrick for his help with preparation of microfluidic channels, and the group of Prof Juntao Li, Sun Yat-Sen University, Guangzhou, China, for providing the thin film silicon samples.

REFERENCES

1. K. Dholakia and T. Čižmár, Nat. Photonics **5**, 335 (2011).
2. C. H. Sow, A. A. Bettiol, Y. Lee, F. C. Cheong, C. T. Lim, and F. Watt, Appl. Phys. B **78**, 705 (2004).
3. F. Merenda, J. Rohner, J.-M. Fournier, and R. P. Salathé, Opt. Express **15**, 6075 (2007).
4. H. Rubinsztein-Dunlop, A. Forbes, M. V. Berry, et al., J. Opt. **19**, 013001 (2017).
5. X. Li, S. Xiao, B. Cai, Q. He, T. J. Cui, and L. Zhou, Opt. Lett. **37**, 4940 (2012).
6. D. Lin, P. Fan, E. Hasman, and M. L. Brongersma, Science **345**, 298 (2014).
7. A. Arbabi, Yu Horie, M. Bagheri, and A. Faraon, Nat. Nanotechnol. **10**, 937 (2015).
8. M. Khorasaninejad and F. Capasso, Science **358** (2017).
9. S. Fan and J. D. Joannopoulos, Phys. Rev. B **65**, 235112 (2002).
10. M. G. Moharam and T. K. Gaylord, J. Opt. Soc. Am. **71**, 811 (1981).
11. A. B. Klemm, D. Stellinga, E. R. Martins, L. Lewis, G. Huyet, L. O'Faolain, and T. F. Krauss, Opt. Lett. **38**, 3410 (2013).
12. A. B. Klemm, D. Stellinga, E. R. Martins, L. Lewis, L. O'Faolain, and T. F. Krauss, Proc. of SPIE **8995**, 89950L (2014).
13. T. A. Nieminen, V. L. Y. Loke, A. B. Stilgoe, G. Knöner, A. M. Brańzyk, N. R. Heckenberg, and H. Rubinsztein-Dunlop, J. Opt. A **9**, S196 (2007).
14. B. Redding and Y.-L. Pan, Opt. Lett. **40**, 2798 (2015).
15. D. Barredo, S. de Léséleuc, V. Lienhard, T. Lahaye, and A. Browaeys, Science **354**, 1021 (2016).